J. Fluid Mech. (2019), *vol.* 875, *pp.* 781–806.
doi:10.1017/jfm.2019.478

Acoustic microstreaming near a plane wall due to a pulsating free or coated bubble: velocity, vorticity and closed streamlines

Nima Mobadersany[1] **and Kausik Sarkar**[1,†]

[1]Department of Mechanical and Aerospace Engineering, George Washington University, Washington, DC 20052, USA

(Received 30 July 2018; revised 10 June 2019; accepted 10 June 2019)

Acoustic microstreaming due to an oscillating microbubble, either coated or free, is analytically investigated. The detailed flow field is obtained and the closed streamlines of the ring vortex generated by microstreaming are plotted in both Eulerian and Lagrangian descriptions. Analytical expressions are found for the ring vortex showing that its length depends only on the separation of the microbubble from the wall and the dependence is linear. The circulation as a scalar measure of the vortex is computed quantitatively identifying its spatial location. The functional dependence of circulation on bubble separation and coating parameters is shown to be similar to that of the shear stress.

Key words: bubble dynamics, cavitation

1. Introduction

An acoustic wave propagating through a medium can generate a steady streaming flow, in addition to the sinusoidal movement of the fluid particles, especially near vibrating elements and bounding walls (Nyborg 1953, 1958; Riley 2001; Tho, Manasseh & Ooi 2007). Streaming flows when associated with an acoustically excited microbubble are called microstreaming. They have been observed near a surface (Kolb & Nyborg 1956), and implicated in numerous harmful and beneficial bioeffects – haemolysis (bursting of red blood cells) (Rooney 1970; Marmottant & Hilgenfeldt 2003; Pommella *et al.* 2015), sonoporation (transient pore formation on cell walls under ultrasound excitation) (Fan, Kumon & Deng 2014; Aliabouzar, Zhang & Sarkar 2016), drug delivery (Lentacker, De Smedt & Sanders 2009) and bone healing (Katiyar, Duncan & Sarkar 2014; Aliabouzar *et al.* 2016; Zhou *et al.* 2016; Aliabouzar *et al.* 2018) – as well as in microfluidics transport (Wang, Jalikop & Hilgenfeldt 2012), micromixing and acoustic cleaning (Liu & Wu 2009; Orbay *et al.* 2016). There have also been extensive theoretical and numerical studies elucidating the phenomena (Nyborg 1958; Wu & Du 1997; Riley 2001; Doinikov & Bouakaz 2010*a*,*b*, 2014; Rallabandi, Wang & Hilgenfeldt 2014; Mobadersany & Sarkar 2018). Recent theoretical studies mostly focused on either the streaming motion near an

† Email address for correspondence: sarkar@gwu.edu

oscillating bubble in the bulk (Wu & Du 1997; Liu & Wu 2009; Doinikov & Bouakaz 2010*a*,*b*) – which might be enhanced due to the presence of a distant wall (Doinikov & Bouakaz 2014) – or the motion near an oscillating bubble attached to the wall (Rallabandi *et al.* 2014, 2015). Here, we investigate the streaming motion, specifically the closed circular streamlines, due to the periodic oscillations of a bubble near but detached from a plane wall revisiting the classical analysis of Nyborg (Nyborg 1958).

Lord Rayleigh (Rayleigh 1945) provided the first theoretical explanation of the acoustic streaming phenomena observed in Kundt's tube as arising from the time-averaged nonlinear advection terms, $-\rho\langle \boldsymbol{u}^{(1)}\cdot\boldsymbol{\nabla}\boldsymbol{u}^{(1)}\rangle_t$ (ρ is density) due to small oscillatory motion $\boldsymbol{u}^{(1)}$, acting as an inhomogeneous forcing term for the second-order equation of motion. This was followed in the 1950s by a series of pioneering studies (Westervelt 1953; Nyborg 1958; Lighthill 1978) that strengthened its theoretical underpinning. Specifically, Nyborg provided a generalized perturbative analysis of the streaming velocity near a boundary and offered expressions for the induced stresses under various conditions, which have been widely used in the literature. Most often an average expression of shear stress – $\mu u_L/\delta$, where μ is the viscosity, ρ the density, $\delta=\sqrt{\mu/\pi\rho f}$ the Stokes boundary layer thickness, f the frequency and u_L the limiting streaming velocity at the edge of the boundary layer – was used. Rooney (1970) experimentally observed haemolysis of red blood cells due to a pulsating (20 kHz) cylindrical bubble (260 μm) resting on a surface, and used this expression along with a point source in a wall representation of the bubble to determine the critical shear stress (∼4500 dyn cm^{-2}) for haemolysis. Lewin & Bjorno (1982) computed the motion of micrometre-sized bubbles excited at megahertz frequencies using the Rayleigh–Plesset equation, and used the Nyborg expression to estimate a streaming shear stress of 1.3 kPa on the attached cell membranes with bubble radius of 1 μm and 20 kPa–3.6 MHz stimulation. Wu (2002) used a modified Rayleigh–Plesset equation with a shell model due to de Jong, Cornet & Lancee (1994) and the same expression to show that it can predict a shear stress (∼12 Pa) in the streaming field of an Optison contrast microbubble at ∼0.1 MPa and 1 or 2 MHz excitation, which is sufficient for reparable sonoporation in a living cell. Forbes & O'Brien (2012) used a similar analysis using the Marmottant model (Marmottant *et al.* 2005) for the shell to predict an increase of sonoporation activity with excitation, maximum sonoporation and its drop-off after collapse.

Wu & Du (1997) computed the microstreaming flow field inside and outside an isolated microbubble oscillating in the field of a plane ultrasound wave by accounting for the monopole volume pulsation and the dipole translation motion in the spherical geometry. The results later were further generalized by removing restrictions on bubble size relative to the wavelength and considering viscous effects in the whole domain (Doinikov & Bouakaz 2010*a*,*b*). Detailed analytical theories have also been developed by Doinikov & Bouakaz (2014) to show that the microstreaming near an oscillating bubble increases considerably due to the presence of a distant rigid wall or in the presence of a second bubble (Doinikov & Bouakaz 2016), especially when they are driven at their resonance frequency.

Here, we consider microstreaming near a rigid wall due to a nearby oscillating microbubble detached from a nearby rigid wall. Krasovitski & Kimmel (2004) were the first to consider such a case; they used an axisymmetric boundary element method to obtain the first-order oscillating potential flow $\boldsymbol{u}^{(1)}$ and then they used the Nyborg expression to compute the shear stress on the plane wall. Recognizing that typically the streaming motion is generated by small-amplitude oscillation, Doinikov & Bouakaz (2010*a*,*b*) used the linearized Rayleigh–Plesset equation to obtain the

first-order velocity in a pioneering theoretical study of sonoporation. They also used the Nyborg expression to compute the shear stress, and under a number of reasonable assumptions provided an expression for sonoporation efficiency in a bubble-cell suspension. However, none of the past studies investigated closed streamlines of the microstreaming flow field near the wall due to a detached oscillating bubble. On the other hand, an array of different streaming motions have been observed with varying viscosity and excitation amplitude (Elder 1959), including flow direction reversal or secondary inner circulation over a vibrating tip (Kolb & Nyborg 1956). Different streaming flows – vortex, dipolar or quadrupolar – were observed for a larger (radius 230–270 μm) bubble excited at lower (2–9 kHz) frequencies (Tho *et al.* 2007; Collis *et al.* 2010; Thameem, Rallabandi & Hilgenfeldt 2016). Collis *et al.* argued that a streaming motion pattern can be utilized to improve sonoporation and sonothrombolysis. Miller (1988) noted a streaming flow radially inward over an ultrasonically activated micropore, rather than outward as expected from the theory. For a two-dimensional bubble attached to a wall, detailed analysis and experiments showed both 'fountain' (streamlines inward at the wall) and 'anti-fountain' (streamlines outward at the wall) flows are possible depending on the excitation frequency (Rallabandi *et al.* 2014). Such diversity of streaming motions and their possible applications in medical and microfluidic technology underscore the importance of a detailed study of the streamline pattern.

In this study, we offer an analytical description of the streamlines due to a free as well as a coated ultrasound contrast microbubble undergoing small-amplitude oscillation near a rigid plane wall, investigating the dependence of the phenomenon on different flow parameters. Given the importance of Nyborg's classic analysis of the streaming phenomenon, his results were obtained recasting the analysis in the standard terminology of the modern perturbation method justifying in detail the order of various terms, and their retention and elimination. The novelty of the present study stems from the computation of the vertical component of the streaming velocity that has been used to plot for the first time the closed Eulerian and Lagrangian streamlines of the vortex structure of the microstreaming flows along the wall for both free and coated bubbles. The length and width of the vortex structure were studied relating them to the flow geometry. An objective vortex identification scheme, the d-2 method (Vollmers 2001), is used to determine the spatial extent of the vortex and the circulation. The variation of circulation and vorticity was related to that of the shear stress at the wall.

2. Mathematical formulation

We investigate the microstreaming phenomenon over a wall due to an oscillating bubble of initial radius R_0 at a distance h from the wall (figure 1). Theoretical analysis of microstreaming solves the governing equations by a perturbative method (Nyborg 1953, 1958):

$$\left.\begin{aligned} \boldsymbol{u} &= \boldsymbol{u}^{(1)} + \boldsymbol{u}^{(2)} + \cdots \\ p &= p^{(1)} + p^{(2)} + \cdots . \end{aligned}\right\} \tag{2.1}$$

The first-order approximation $\boldsymbol{u}^{(1)}$ solves the linearized equation neglecting the nonlinear advection terms and obtains a sinusoidal velocity. To properly understand the perturbative nature of the problem, we note that for a bubble of initial radius R_0 executing oscillation with a small amplitude εR_0, $\varepsilon \ll 1$, $\boldsymbol{u}^{(1)} \sim U = \varepsilon\omega R_0$, $\omega = 2\pi f$.

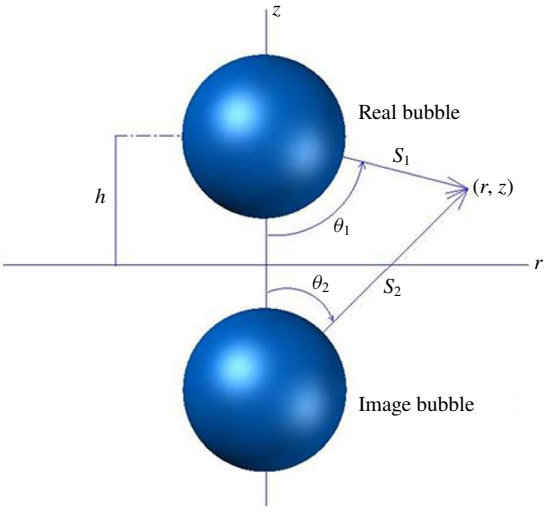

FIGURE 1. (Colour online) Schematic of the problem.

At the second order, the convective nonlinear term, quadratic product of $\boldsymbol{u}^{(1)}$, appears as a forcing term, with the equation upon averaging becoming

$$\mu\nabla^2\langle\boldsymbol{u}^{(2)}\rangle_t - \boldsymbol{\nabla}\langle p^{(2)}\rangle_t = \boldsymbol{F} = \rho\langle\boldsymbol{u}^{(1)}\cdot\boldsymbol{\nabla}\boldsymbol{u}^{(1)}\rangle_t, \tag{2.2}$$

with ρ and μ being the fluid intensity and viscosity. Here $\langle\,\rangle_t$ is the average over the time period of the oscillating excitation. Note that the resulting streaming motion has been named Rayleigh–Nyborg–Westervelt streaming by Lighthill (1978) in contrast to Stuart streaming (Stuart 1966). The underlying approximation is only valid when bubble streaming Reynolds number Re_{bs} is small. In anticipation of the streaming velocity $\sim U^2/\omega R_0$ (see equation (2.22) below) and the length scale $\delta = \sqrt{2\nu/\omega}$ ($\nu = \mu/\rho$), one obtains (Davidson & Riley 1971; Marmottant & Hilgenfeldt 2003) $Re_{bs} = \varepsilon^2(2\omega R_0^2/\nu)^{1/2} = \varepsilon^2(2Re_b)^{1/2}$, with $Re_b = \omega R_0^2/\nu$ being the Reynolds number of the bubble motion. We will later show that Re_{bs} is small in the present case.

An oscillating bubble near a wall experiences a secondary attractive Bjerknes force towards the wall due to the wall-induced image bubble. The force is second order in nature and would introduce a translation towards the wall. We have neglected this effect here as was done in many studies in the literature (Doinikov & Bouakaz 2014). Batchelor (1967) offered a potential flow estimation of the force using the virtual mass $2\rho\pi R_0^3/3$ of the bubble situated at distance h from the wall to be $\varepsilon^2\pi\rho\omega^2R_0^6/(2h^2)$. Equating with the Stokes drag, one obtains a velocity of $U/\omega R_0 = \varepsilon^2 Re_b/[12(h/R)^2]$. For sufficiently small ε and large h/R (these are also the assumptions for this analysis of Bjerknes force to be valid), this velocity remains small for the stationary bubble assumption adopted here to be valid. The boundary layer being $\delta = \sqrt{2\nu/\omega}$, the steady viscous streaming field examined here can be expected to be established within a few time periods ($\sim\omega^{-1}$) as was observed in experiment (personal communication with Professor Rallabandi). Close to the wall, the bubble oscillation would cease to be spherical; it would experience shape oscillations and complex streaming patterns that, in the case of a drug-loaded contrast microbubble, can enhance the transport of drugs (Lajoinie *et al.* 2018).

Averaging the quadratic term in (2.2) gives rise to a steady force that drives the streaming motion. Nyborg (1958) noted that the formal solution of this problem requires that boundary conditions be satisfied on the exact boundary, which is possible only for simple boundaries (plane, hemisphere, etc.) with the simplest velocity distributions on them (see Fabre *et al.* (2017) where the authors had to resort to finite-element solution for the first- and the second-order problems between two spheres). For a more general situation, Nyborg sought an alternative method. Following an earlier investigation of Schlicting (1979), he made a key observation that one does not need the solution for the entire region (with dimension L, here equal to R_0), but only in the near-boundary region (dimension δ). With a number of ingenious approximations, Nyborg was able to obtain an expression of the streaming motion that depends on the surface values of the potential part of the first-order velocity. Nyborg's description of the pioneering work was often terse, intuitive without adequate reasoning for the assumed order of the terms and their retention, and based on a formulation with a finite sound speed later simplified using an 'approximate incompressibility' assumption. Furthermore, it was solved in Cartesian coordinates allowing modifications for slight curvilinearity. We provide a description of the mathematical derivation in radial coordinates under the assumption of axisymmetry detailing the various approximations which would be helpful for understanding several key features of the perturbative approach.

2.1. *Linear oscillatory field at first order*

The fluid velocity and pressure $\boldsymbol{u}(\boldsymbol{x}, t)$ and pressure $p(\boldsymbol{x}, t)$ solve the Navier–Stokes equation

$$\left.\begin{gathered}\frac{\partial \boldsymbol{u}}{\partial t}+\boldsymbol{u}\cdot\boldsymbol{\nabla}\boldsymbol{u}=-\frac{1}{\rho}\boldsymbol{\nabla}p+\nu\nabla^2\boldsymbol{u},\\ \boldsymbol{\nabla}\cdot\boldsymbol{u}=0,\end{gathered}\right\} \tag{2.3}$$

with $\nu=\mu/\rho$ being the kinematic viscosity. With the perturbation expansion (2.1), and using a time-periodic expression for the first-order field

$$\boldsymbol{u}^{(1)}(\boldsymbol{x}, t)=\boldsymbol{u}_1(\boldsymbol{x})\mathrm{e}^{\mathrm{i}\omega t}, \quad p^{(1)}(\boldsymbol{x}, t)=p_1(\boldsymbol{x})\mathrm{e}^{\mathrm{i}\omega t}, \tag{2.4a,b}$$

one obtains for the momentum equation at $O(\varepsilon)$

$$\mathrm{i}\omega\boldsymbol{u}_1=-\frac{1}{\rho}\boldsymbol{\nabla}p_1+\nu\nabla^2\boldsymbol{u}_1. \tag{2.5}$$

Equation (2.5) is solved using a Helmholtz decomposition

$$\boldsymbol{u}_1=\boldsymbol{u}_\varphi+\boldsymbol{u}_A, \quad \boldsymbol{u}_\varphi=\boldsymbol{\nabla}\varphi, \quad \nabla^2\varphi=0, \quad \boldsymbol{u}_A=\boldsymbol{\nabla}\times A, \quad \boldsymbol{\nabla}\cdot A=0. \tag{2.6a–e}$$

Note that the generality of the Nyborg formulation (Nyborg 1958) is premised on finding the velocity in terms of values of the potential component $\boldsymbol{u}_\varphi$ and its derivative at the boundary. The vortical part $\boldsymbol{u}_A$ satisfies

$$(\nabla^2+H^2)\boldsymbol{u}_A, \quad H^2=-\mathrm{i}\omega/\nu, \quad H=(1-\mathrm{i})\sqrt{\frac{\omega}{2\nu}}=(1-\mathrm{i})\beta, \tag{2.7a–c}$$

where the sign of H was chosen for decaying solution of $\exp(-\mathrm{i}Hz)$. The solution has the typical structure of Stokes boundary layer for an oscillatory outer driving flow $\boldsymbol{u}_\varphi$ (of order $\sim U$ and varying in a large scale $\sim L$) near a wall with boundary layer thickness $\delta = 1/\beta \ll L$. We seek solution (u, w) in an axisymmetric geometry. Accordingly, the solution of the radial component u_A is straightforward and chosen to ensure a zero tangential velocity countering u_φ as

$$u_A = -u_\varphi \mathrm{e}^{-\mathrm{i}Hz}. \tag{2.8}$$

It satisfies (2.7). The axial component w_A is chosen as

$$w_A = -\frac{\Gamma}{\mathrm{i}h}\mathrm{e}^{-\mathrm{i}Hz}, \quad \Gamma = -\frac{\partial w_\varphi}{\partial z} = \frac{1}{r}\frac{\partial}{\partial r}(ru_\varphi). \tag{2.9a,b}$$

Due to (2.6), w_φ and Γ are harmonic, and therefore (2.9) satisfies (2.7). We note that

$$\boldsymbol{\nabla}\cdot\boldsymbol{u}_\varphi = \frac{1}{r}\frac{\partial}{\partial r}(ru_\varphi) + \frac{\partial w_\varphi}{\partial z} = 0, \tag{2.10}$$

to obtain

$$\boldsymbol{\nabla}\cdot\boldsymbol{u}_A = -\frac{1}{r}\frac{\partial}{\partial r}(ru_\varphi)\mathrm{e}^{-\mathrm{i}Hz} - \frac{\partial w_\varphi}{\partial z}\mathrm{e}^{-\mathrm{i}Hz} + \frac{1}{\mathrm{i}H}\frac{\partial^2 w_\varphi}{\partial z^2}\mathrm{e}^{-\mathrm{i}Hz} \approx 0, \tag{2.11}$$

the last term being higher order in the small quantity δ/L compared to the first two terms and therefore was neglected here as well as below (effectively Γ being treated as approximately a constant). The velocity $\boldsymbol{u}_\varphi + \boldsymbol{u}_A$ however does not satisfy the zero normal velocity condition at $z = 0$ due to w_A. Correcting for that, a modified total first-order velocity is found as

$$\boldsymbol{u} = \boldsymbol{u}_\varphi + \boldsymbol{u}_A + w_c\hat{\boldsymbol{e}}_z, \quad w_c = \Gamma/\mathrm{i}H, \tag{2.12a,b}$$

keeping in mind that the non-decaying w_c is only meaningful while considering the velocity field in the small boundary layer region. Therefore, one obtains the time-periodic first-order velocity field (superscript $^{(1)}$ indicates the corresponding term with periodic time dependence included):

$$\left.\begin{aligned} u^{(1)} = u_\varphi^{(1)} + u_A^{(1)} &= u_\varphi[\cos\omega t - \mathrm{e}^{-\beta z}\cos(\omega t - \beta z)], \\ w^{(1)} = w_\varphi^{(1)} + w_c^{(1)} + w_A^{(1)} &= w_\varphi\cos\omega t \\ &\quad + \frac{\Gamma}{\sqrt{2}\beta}[\cos(\omega t - \pi/4) - \mathrm{e}^{-\beta z}\cos(\omega t - \beta z - \pi/4)]. \end{aligned}\right\} \tag{2.13}$$

This expression is consistent with Nyborg (1958).

2.2. *Streaming at second order*

At the second order, one observes the forcing term $\boldsymbol{F}$ on the right-hand side of the average Stokes equation (2.2). As was noted by Nyborg, quadratic product of the irrotational part $\boldsymbol{u}_\varphi = \boldsymbol{\nabla}\varphi$ does not contribute to streaming and can balance the pressure gradient term as in Bernoulli term

$$-\boldsymbol{\nabla}p_2 = \boldsymbol{u}_\varphi\cdot\boldsymbol{\nabla}\boldsymbol{u}_\varphi = \tfrac{1}{2}\boldsymbol{\nabla}(|\boldsymbol{\nabla}\varphi|^2), \tag{2.14}$$

reducing (2.2) into

$$\mu\nabla^2\langle \boldsymbol{u}^{(2)}\rangle_t = \boldsymbol{F} = \rho\langle(\boldsymbol{u}_A^{(1)} + w_c^{(1)}\hat{e}_z)\cdot\nabla\boldsymbol{u}_\varphi^{(1)} + \boldsymbol{u}^{(1)}\cdot\nabla(\boldsymbol{u}_A^{(1)} + w_c^{(1)}\hat{e}_z)\rangle_t. \tag{2.15}$$

Therefore, the forcing term in the r-direction becomes

$$\begin{aligned} F_r &= \rho\langle \boldsymbol{u}_A^{(1)}\cdot\nabla u_\varphi^{(1)} + w_c^{(1)}\hat{e}_z\cdot\nabla u_\varphi^{(1)} + \boldsymbol{u}^{(1)}\cdot\nabla u_A^{(1)}\rangle_t \\ &= \rho\,\langle u_A^{(1)}\partial_r u_\varphi^{(1)} + w_A^{(1)}\partial_z u_\varphi^{(1)} + w_c^{(1)}\partial_z u_\varphi^{(1)} \\ &\quad + u_\varphi^{(1)}\partial_r u_A^{(1)} + u_A^{(1)}\partial_r u_A^{(1)} + w_\varphi^{(1)}\partial_z u_A^{(1)} + w_c^{(1)}\partial_z u_A^{(1)} + w_A^{(1)}\partial_z u_A^{(1)}\rangle_t. \end{aligned} \tag{2.16}$$

Noting the order of terms

$$\left.\begin{array}{c} u_\varphi \sim u_A \sim U, \\ w_A \sim w_c \sim \delta U/L, \\ \partial_r u_\varphi \sim \partial_z u_\varphi \sim \partial_r u_A \sim U/L, \\ \partial_z u_A \sim U/\delta, \end{array}\right\} \tag{2.17}$$

and neglecting higher order in δ/L, we obtain

$$F_r = \rho\langle u_A^{(1)}\partial_r u_\varphi^{(1)} + u_\varphi^{(1)}\partial_r u_A^{(1)} + u_A^{(1)}\partial_r u_A^{(1)} + w^{(1)}\partial_z u_A^{(1)}\rangle_t. \tag{2.18}$$

Each term on the right-hand side is $O(U^2/L)$. In an effort to express each term in terms of u_φ and $\partial_r u_\varphi^{(1)}$, following Nyborg, we express the odd term w_φ in (2.13) as

$$w_\varphi \approx z\left(\frac{\partial w_\varphi}{\partial z}\right)_{z=0} = -\frac{z}{r}\left[\frac{\partial}{\partial r}(ru_\varphi)\right]_{z=0}. \tag{2.19}$$

Note that with (2.19) $w_\varphi \sim \delta U/L$ and therefore $w_\varphi^{(1)}\partial_z u_A^{(1)}$ in (2.18) is also $O(U^2/L)$ consistent with the other terms there. After substituting (2.13) in (2.18) averaging over time, one obtains

$$\begin{aligned} F_r &= \frac{\rho}{2}\,(u_\varphi\partial_r u_\varphi(\mathrm{e}^{-2\beta z} - 2\mathrm{e}^{-\beta z}\cos\beta z) \\ &\quad - u_\varphi(1/r)\partial_r(ru_\varphi)\mathrm{e}^{-\beta z}\{\beta z(\cos\beta z + \sin\beta z) - \sin\beta z\}). \end{aligned} \tag{2.20}$$

In the governing equation (2.15) in the second order, we note that the vertical (z) derivative is larger than the transverse (r) derivative by $O(L/\delta)$ to obtain

$$\left\langle \frac{\partial^2 u^{(2)}}{\partial^2 z}\right\rangle_t = -\frac{F_r}{\mu}. \tag{2.21}$$

Integrating and noting (2.9), we get

$$\left.\begin{array}{c} \langle u^{(2)}\rangle_t = \dfrac{1}{\omega}\left(\dfrac{1}{2}\dfrac{\partial u_\varphi^2}{\partial r}(u_\alpha - u_\beta) - \dfrac{u_\varphi^2}{r}u_\beta\right), \quad \text{where} \\ u_\alpha = \dfrac{1}{4}\mathrm{e}^{-2\beta z} + \mathrm{e}^{-\beta z}\sin\beta z - \dfrac{1}{4}, \\ u_\beta = \dfrac{1}{2}\beta z\mathrm{e}^{-\beta z}(\cos\beta z - \sin\beta z) - \mathrm{e}^{-\beta z}\left(\sin\beta z + \dfrac{1}{2}\cos\beta z\right) + \dfrac{1}{2}, \end{array}\right\} \tag{2.22}$$

as was also found by Nyborg (1958).

The vertical component of streaming velocity $\langle w^{(2)}\rangle_t$ – not found in the literature but critical for plotting streamlines – is obtained by using the equation of mass conservation and taking into account the no-slip condition on the rigid wall:

$$\begin{aligned}\langle w^{(2)}\rangle_t &= \int_0^z -\frac{1}{r}\frac{\partial(r\langle u^{(2)}\rangle)}{\partial r}\,\mathrm{d}z \\ &= -\frac{1}{2\omega}\left(\frac{1}{r}\frac{\partial u_\varphi^2}{\partial r}\right) \\ &\quad\times\left(-\frac{1}{8\beta}\mathrm{e}^{-2\beta z}-\frac{1}{4\beta}\mathrm{e}^{-\beta z}(6\beta z\sin\beta z+8\sin\beta z+14\cos\beta z)-\frac{7}{4}z+\frac{29}{8\beta}\right) \\ &\quad-\frac{1}{2\omega}\left(\frac{\partial^2 u_\varphi^2}{\partial r^2}\right) \\ &\quad\times\left(-\frac{1}{8\beta}\mathrm{e}^{-2\beta z}-\frac{1}{4\beta}\mathrm{e}^{-\beta z}(2\beta z\sin\beta z+4\sin\beta z+6\cos\beta z)-\frac{3}{4}z+\frac{13}{8\beta}\right). \quad (2.23)\end{aligned}$$

Here the z-dependence of $\partial u_\varphi^2/\partial r$ and $\partial^2 u_\varphi^2/\partial r^2$ is neglected in the boundary layer similar to what was assumed in (2.20). The acoustic streaming velocity field is therefore known in terms of the outer irrotational velocity field. One can compute the shear stress on the wall (Nyborg 1958) as

$$\tau_{wall} = \mu\frac{\partial\langle u^{(2)}\rangle_t}{\partial z}\bigg|_{z=0} = \frac{\rho_0}{4\beta}u_\varphi\frac{\partial u_\varphi}{\partial r}\bigg|_{z=0}. \quad (2.24)$$

2.3. *Lagrangian streaming velocity*

For comparison with the average path of a tracer particle, it was noted before that one would also need to find the Lagrangian or particle-averaged streaming velocity (Nyborg 1958) which contains an additional Stokes drift term

$$\langle \boldsymbol{u}_T\rangle_t = \left\langle\left(\int \boldsymbol{u}^{(1)}\,\mathrm{d}t\right)\cdot\boldsymbol{\nabla}\boldsymbol{u}^{(1)}\right\rangle_t, \quad (2.25)$$

expressed in terms of the first-order velocity given in (2.13). For the radial component, one can obtain

$$\begin{aligned}\langle u_T^{(1)}\rangle_t &= \left\langle\left(\int u^{(1)}\,\mathrm{d}t\right)\partial_r u^{(1)}\right\rangle_t + \left\langle\left(\int w_\varphi^{(1)}\,\mathrm{d}t\right)\partial_z u_\varphi^{(1)}\right\rangle_t + \left\langle\left(\int w_A^{(1)}\,\mathrm{d}t\right)\partial_z u_\varphi^{(1)}\right\rangle_t \\ &\quad+\left\langle\left(\int w_c^{(1)}\,\mathrm{d}t\right)\partial_z u_\varphi^{(1)}\right\rangle_t + \left\langle\left(\int w_\varphi^{(1)}\,\mathrm{d}t\right)\partial_z u_A^{(1)}\right\rangle_t + \left\langle\left(\int w_A^{(1)}\,\mathrm{d}t\right)\partial_z u_A^{(1)}\right\rangle_t \\ &\quad+\left\langle\left(\int w_c^{(1)}\,\mathrm{d}t\right)\partial_z u_A^{(1)}\right\rangle_t. \quad (2.26)\end{aligned}$$

Using (2.19) and (2.17), we realize that the second, third and fourth terms involving

$\partial_z u_\varphi^{(1)}$ are higher order in the small quantity δ/L than the others. The first term is identically zero. We obtain

$$\langle u_T\rangle_t = \frac{1}{2\omega}\left(\frac{1}{2}\frac{\partial u_\varphi^2}{\partial r}+\frac{u_\varphi^2}{r}\right)u_\varepsilon,$$
$$\text{where } u_\varepsilon = \beta z \mathrm{e}^{-\beta z}(\cos\beta z-\sin\beta z)-\mathrm{e}^{-\beta z}\cos\beta z+\mathrm{e}^{-2\beta z}. \quad (2.27)$$

Nyborg (1958) stressed that the vertical component is much smaller. However, it is critical for computing the streamlines and can be found by using continuity:

$$\langle w_T\rangle_t = \int_0^z -\frac{1}{r}\frac{\partial(r\langle u_T\rangle)}{\partial r}\,\mathrm{d}z$$
$$= \frac{1}{4\omega\beta}\left(\frac{1}{2}\frac{\partial^2 u_\varphi^2}{\partial r^2}+\frac{3}{2r}\frac{\partial u_\varphi^2}{\partial r}\right)(-2\beta z\mathrm{e}^{-\beta z}\sin\beta z-2\mathrm{e}^{-\beta z}\cos\beta z+\mathrm{e}^{-2\beta z}+1). \quad (2.28)$$

Note that Raney, Corelli & Westervelt (1954) found that adding this correction improved the comparison of theory with experimental observation of streaming near a cylinder.

2.4. *Potential velocity u_φ due to oscillating bubble above a rigid surface*

The problem of a bubble of initial radius R_0 near a plane rigid wall at a distance h from the wall is equivalent to two bubbles of the same initial radius separated by a distance of $2h$; it satisfies the impermeability condition in the plane of the rigid wall.

The velocity potential ϕ of the fluid around the microbubble is

$$\varphi = -\left(\frac{1}{S_1}+\frac{1}{S_2}\right)\dot{R}R^2, \quad (2.29)$$

where S_1 and S_2 are the distances from the centre of the real and image microbubbles to the desired location in the fluid and $\dot{R}$ and R are the velocity and instantaneous radius of the microbubble. The radial and vertical components of the irrotational velocity $\nabla\varphi$ are

$$\left.\begin{aligned} u^{(\varphi)} &= u_\varphi\cos\omega t = \dot{R}R^2\left(\frac{r}{(r^2+(z-h)^2)^{3/2}}+\frac{r}{(r^2+(z+h)^2)^{3/2}}\right),\\ w^{(\varphi)} &= w_\varphi\cos\omega t = \dot{R}R^2\left(\frac{z-h}{(r^2+(z-h)^2)^{3/2}}+\frac{z+h}{(r^2+(z+h)^2)^{3/2}}\right).\end{aligned}\right\} \quad (2.30)$$

Here u_φ and w_φ are time-independent parts of the potential velocity components in radial and vertical directions and r and z are the radial and vertical coordinates. The instantaneous bubble radius R and velocity $\dot{R}$ are described by the Rayleigh–Plesset-type equation

$$\left.\begin{aligned} \rho\left(R\ddot{R}+\frac{3}{2}\dot{R}^2\right) &= P_b-P_0+P_{ex}\sin\omega t,\\ P_b = P_{g_0}\left(\frac{R_0}{R}\right)^{3\kappa}-\frac{4\mu\dot{R}}{R}-\frac{2\gamma}{R}-P_{sc}(h,t),&\\ P_{sc}(h,t) = \rho\frac{R}{2h}(R\ddot{R}+2\dot{R}^2).&\end{aligned}\right\} \quad (2.31)$$

Here P_b is the fluid pressure adjacent to the microbubble, P_0 is the ambient pressure (100 kPa) and P_{ex} is the ultrasound excitation amplitude. Parameter γ is the gas–fluid surface tension, P_{g_0} is the initial gas pressure inside the microbubble and κ is the polytropic constant. Note that the impermeability at the wall is accounted for by the effect of the wall being considered as a pressure $P_{sc}(h, t)$ scattered from the image bubble located at a distance $2h$ from the real bubble.

2.5. *Linearized bubble dynamics and streaming fields*

Assuming that the microbubble is pulsating with a small amplitude $R = R_0(1 + x)$, equation (2.31) is linearized in x. Non-dimensionalizing t and P_{ex} as $t^* = t\omega$ and $P^*_{ex} = P_{ex}/P_0$ results in an equation of damped harmonic oscillator

$$\ddot{x} + \left(\frac{4}{Re_b(1 + R_0/2h)}\right)\dot{x} + \left(\frac{3\kappa Eu_b}{1 + R_0/2h} + \frac{6\kappa - 2}{We_b(1 + R_0/2h)}\right)x = \frac{P^*_{ex}Eu_b \sin(\omega t)}{1 + R_0/2h}, \tag{2.32}$$

where

$$Re_b = \frac{\rho R_0^2\omega}{\mu}, \quad Eu_b = \frac{P_0}{\rho R_0^2\omega^2}, \quad We_b = \frac{\rho R_0^3\omega^2}{\gamma}, \tag{2.33a–c}$$

are the characteristic Reynolds (we have taken $R_0\omega$ as the velocity scale), Euler and Weber numbers. And

$$\left.\begin{aligned} \frac{\omega_0^2}{\omega^2} &= \frac{3\kappa Eu_b + (6\kappa - 2)/We_b}{(1 + R_0/2h)}, \\ \delta_t &= \frac{4\omega}{Re_b(1 + R_0/2h)\omega_0}, \end{aligned}\right\} \tag{2.34}$$

where ω_0 and δ_t are the circular natural frequency and the damping term of the microbubble. Note that the natural frequency is modified due to the presence of the wall by the factor $(1 + R_0/2h)^{-1}$. The analytical solution of equation (2.32) in the steady region is

$$x = \frac{Eu_bP^*_{ex}\sin(\omega t + \phi)}{Z_m(1 + R_0/2h)} = \xi_m \sin(\omega t + \phi), \tag{2.35}$$

where $Z_m = \sqrt{(\delta_t\omega_0/\omega)^2 + (1/\omega^4)(\omega_0^2 - \omega^2)^2}$ is the non-dimensional absolute value of impedance and ϕ is the oscillation phase that can be absorbed by redefining time as $t' = t^* + \phi/\omega$. As a result the irrotational velocity u_φ from equation (2.30), when non-dimensionalized by $R_0\omega$, becomes

$$u_\varphi^* = \frac{\xi_m}{r^{*2}} \left(\frac{1}{\left(1+\left(\frac{z^*-h^*}{r^*}\right)^2\right)^{3/2}} + \frac{1}{\left(1+\left(\frac{z^*+h^*}{r^*}\right)^2\right)^{3/2}} \right)\Bigg|_{z*=0}$$
$$= \frac{2\xi_m}{r^{*2}\left(1+\left(\frac{h^*}{r^*}\right)^2\right)^{3/2}}, \tag{2.36}$$

$$\frac{\partial u_\varphi^*}{\partial r^*} = \frac{\xi_m}{r^{*3}\left(1+\left(\frac{z^*-h^*}{r^*}\right)^2\right)^{3/2}} \left(\frac{3}{\left(\frac{z^*-h^*}{r^*}\right)^2\left(1+\left(\frac{z^*-h^*}{r^*}\right)^2\right)} - 2 \right)\Bigg|_{z=0}$$
$$+ \frac{\xi_m}{r^{*3}\left(1+\left(\frac{z^*+h^*}{r^*}\right)^2\right)^{3/2}} \left(\frac{3}{\left(\frac{z^*+h^*}{r^*}\right)^2\left(1+\left(\frac{z^*+h^*}{r^*}\right)^2\right)} - 2 \right)\Bigg|_{z=0}$$
$$= \frac{2\xi_m}{r^{*3}\left(1+\left(\frac{h^*}{r^*}\right)^2\right)^{3/2}} \left(\frac{3}{\left(\frac{h^*}{r^*}\right)^2\left(1+\left(\frac{h^*}{r^*}\right)^2\right)} - 2 \right), \tag{2.37}$$

with a similar expression for w_φ^*. Note that in conformity with the approximation that u_φ^* varies in a larger scale (h and R_0) compared to the boundary layer thickness δ, the expressions were evaluated at the wall $z=0$. Correspondingly, shear stress (2.24) non-dimensionalized with respect to P_0 becomes

$$\tau^* = \frac{2\xi_m^2 r^*}{Eu_b(2Re_b)^{1/2}h^{*5}} \frac{(1-2r^{*2}/h^{*2})}{(1+r^{*2}/h^{*2})^4}. \tag{2.38}$$

2.6. *Effects of translation of microbubble*

An oscillating microbubble translates towards the wall due to Bjerknes force as has been carefully analysed by Doinikov & Bouakaz (2014). The velocity potential is modified by an additional dipole term

$$\varphi = -\left(\frac{1}{S_1}+\frac{1}{S_2}\right)\dot{R}R^2 - b\left(\frac{h-z}{S_1^3}+\frac{h+z}{S_2^3}\right). \tag{2.39}$$

Corresponding linearized non-dimensional potential velocity in the radial direction is also modified as

$$u_\varphi^* = \frac{\xi_m}{r^{*2}}\left(\frac{1}{\left(1+\left(\frac{z^*-h^*}{r^*}\right)^2\right)^{3/2}}+\frac{1}{\left(1+\left(\frac{z^*+h^*}{r^*}\right)^2\right)^{3/2}}\right)\Bigg|_{z=0}$$
$$+\frac{b^l}{r^{*4}}\left(\frac{3(h^*-z^*)}{\left(1+\left(\frac{z^*-h^*}{r^*}\right)^2\right)^{5/2}}+\frac{3(h^*+z^*)}{\left(1+\left(\frac{z^*-h^*}{r^*}\right)^2\right)^{5/2}}\right)\Bigg|_{z=0}$$
$$=\frac{2\xi_m}{r^{*2}\left(1+\left(\frac{h^*}{r^*}\right)^2\right)^{3/2}}+\frac{6h^*b^l}{r^{*4}\left(1+\left(\frac{h^*}{r^*}\right)^2\right)^{5/2}}, \tag{2.40}$$

where b^l is given by (Doinikov & Bouakaz 2014)

$$b^l=\left|\frac{\xi_m}{4h^{*2}}\left(\frac{\alpha^3+3\mathrm{i}\alpha^2-6\alpha-6\mathrm{i}}{-\alpha^3-3\mathrm{i}\alpha^2+18\alpha+18\mathrm{i}}\right)\right|, \quad \alpha=(1+\mathrm{i})R_0\beta. \tag{2.41}$$

We note that the faster decay with r^* characteristic of a dipole makes the translational part much smaller at larger radial distance. Also at smaller $r^* \ll 1$, the translational part is smaller than the radial part by a factor of $3/4h^{*3}$. For separation distances of the microbubble from the wall $h \geqslant 2R_0$, this factor is quite small, and therefore the effect of translation here has not been considered, except briefly. However, note that it can easily be accounted for using the expression (2.41).

2.7. *Effects of the shell on a contrast microbubble*

Microbubbles (size ∼1–10 μm) used for contrast-enhanced ultrasound imaging (Goldberg, Raichlen & Forsberg 2001; Paul *et al.* 2014) are coated by a monolayer of lipids, proteins or other surface-active molecules to stabilize them against premature dissolution due to gas diffusion (Katiyar, Sarkar & Jain 2009; Sarkar, Katiyar & Jain 2009). There have been numerous models of contrast microbubble coating (de Jong *et al.* 1992; Church 1995; Hoff, Sontum & Hovem 2000; Chatterjee & Sarkar 2003; Marmottant *et al.* 2005; Sarkar *et al.* 2005; Tsiglifis & Pelekasis 2008; Paul *et al.* 2010). We have recently shown that most of these models can be expressed as an interfacial rheological model with an effective surface tension $\gamma(R)$ and an effective dilatational viscosity $\kappa^s(R)$ (Katiyar & Sarkar 2011). Here we have used a strain-softening model called the exponential elasticity model (Paul *et al.* 2010):

$$\gamma(R)=\gamma_0+\beta^sE^s, \quad E^s=E_0^s\exp(-\alpha^s\beta^s), \quad \beta^s=\left(\frac{R}{R_E}\right)^2-1, \quad \kappa^s \text{ constant}, \tag{2.42a–c}$$

where E^s is the shell dilatational elasticity, β^s is the change in area fraction from the equilibrium radius $R_E=R_0[1+(1-\sqrt{1+4\gamma_0\alpha^s/E_0^s})/2\alpha^s]^{-1/2}$, and γ_0, α^s and E_0^s are

material properties of the coating. We have demonstrated how these characteristic properties for a microbubble contrast agent can be measured through acoustic experiments (Paul *et al.* 2010, 2013; Kumar & Sarkar 2015; Xia, Porter & Sarkar 2015; Kumar & Sarkar 2016). For example, for contrast agent Sonazoid, they are $\gamma_0 = 0.019$ N m^{-1}, $E_0^s = 0.55$ N m^{-1}, $\alpha^s = 1.5$ and $\kappa^s = 1.2 \times 10^{-8}$ N s m^{-1}. As a result of the coating stresses, equations (2.34) become

$$\left.\begin{aligned} \frac{\omega_0^2}{\omega^2} &= \frac{1}{(1+R_0/2h)}\left(3\kappa Eu_b + \frac{2(\sqrt{1+4\gamma_0\alpha^s/E_0^s}/\alpha^s)(1+2\alpha^s-\sqrt{1+4\gamma_0\alpha^s/E_0^s})}{We_b^s}\right), \\ \delta_t &= \frac{4\omega}{(1+R_0/2h)\omega_0}\left(\frac{1}{Re_b}+\frac{1}{Re_b^s}\right), \end{aligned}\right\} \tag{2.43}$$

where $We_b^s = \rho R_0^3\omega^2/E_0^s$, $Re_b^s = \rho R_0^3\omega/\kappa^s$, γ_0/E_0^s and α^s are the non-dimensional numbers related to the coating parameters. We have shown that different models of coating often give rise to qualitatively similar behaviours (Kumar & Sarkar 2015; Xia *et al.* 2015; Kumar & Sarkar 2016) even for nonlinear response. We expect that they would vary very little in their predictions of linear dynamics.

2.8. *Circulation of the ring vortex in microstreaming flow*

Microstreaming gives rise to an axisymmetric vortex ring near the wall (see figure 5). We compute the circulation of the vortex ring, a single quantitative scalar measure of the vortex, in the r–z plane using the Stokes theorem. However, it requires us to objectively define the spatial extent of the vortex. The problem of a quantitative and objective identification of vortices has been a major issue in experimentally measured velocity data in turbulent flows. In fact although vortices are ubiquitous, there is no universally accepted definition of a 'vortex' (Chakraborty, Balachandar & Adrian 2005). The problem can be appreciated by noting that simple shear has vorticity, yet does not contain a vortex. A local method of vortex identification obtains a point function that classifies the point to be outside or inside a vortex. The criterion being completely defined by the local velocity gradient is Galilean invariant. There have been many local methods proposed in the literature and their relative merits, specifically their utility in identifying vortical structures in complex turbulent flow measurements, have been investigated in detail (Chakraborty *et al.* 2005). Here, we apply the d2 method (discriminant of non-real eigenvalues of velocity gradient tensor) (Vollmers 2001) principally for its ease of use in two-dimensional data. It is a Galilean-invariant method that distinguishes vortical structures from boundary layers and shear layers (Najjari & Plesniak 2016). A negative value of d_2 corresponds to the non-real eigenvalue of velocity gradient and indicates a vortex region:

$$d_2 = \left(\frac{\partial\langle u^{(2)}\rangle_t}{\partial r} + \frac{\partial\langle w^{(2)}\rangle_t}{\partial z}\right)^2 - 4\left(\frac{\partial\langle u^{(2)}\rangle_t}{\partial r}\frac{\partial\langle w^{(2)}\rangle_t}{\partial z} - \frac{\partial\langle u^{(2)}\rangle_t}{\partial z}\frac{\partial\langle w^{(2)}\rangle_t}{\partial r}\right), \tag{2.44}$$

where

$$\left.\begin{aligned}
\frac{\partial\langle u^{(2)}\rangle_t}{\partial r} &= \frac{1}{\omega}\left(\frac{1}{2}\frac{\partial^2 u_\varphi^2}{\partial r^2}(u_\alpha - u_\beta) - \left(\frac{\partial u_\varphi^2}{r\partial r} - \frac{u_\varphi^2}{r^2}\right)u_\beta\right),\\
\frac{\partial\langle u^{(2)}\rangle_t}{\partial z} &= \frac{1}{\omega}\left(\frac{1}{2}\frac{\partial u_\varphi^2}{\partial r}\beta \mathrm{e}^{-\beta z}(\cos\beta z - 2\sin\beta z + \beta z\cos\beta z - 0.5\mathrm{e}^{-\beta z})\right.\\
&\quad \left. - \frac{u_\varphi^2}{r}(\beta \mathrm{e}^{-\beta z}(\sin\beta z - \beta z\cos\beta z))\right),\\
\frac{\partial\langle w^{(2)}\rangle_t}{\partial r} &= -\frac{1}{2\omega}\left(-\frac{1}{r^2}\frac{\partial u_\varphi^2}{\partial r} + \frac{1}{r}\frac{\partial^2 u_\varphi^2}{\partial r^2}\right)\\
&\quad \times\left(-\frac{1}{8\beta}\mathrm{e}^{-2\beta z} - \frac{1}{4\beta}\mathrm{e}^{-\beta z}(6\beta z\sin\beta z + 8\sin\beta z + 14\cos\beta z) - \frac{7}{4}z + \frac{29}{8\beta}\right)\\
&\quad - \frac{1}{2\omega}\left(\frac{\partial^3 u_\varphi^2}{\partial r^3}\right)\\
&\quad \times\left(-\frac{1}{8\beta}\mathrm{e}^{-2\beta z} - \frac{1}{4\beta}\mathrm{e}^{-\beta z}(2\beta z\sin\beta z + 4\sin\beta z + 6\cos\beta z) - \frac{3}{4}z + \frac{13}{8\beta}\right),\\
\frac{\partial\langle w^{(2)}\rangle_t}{\partial z} &= -\frac{1}{2\omega}\left(\frac{1}{r}\frac{\partial u_\varphi^2}{\partial r}\right)\\
&\quad \times\left(\frac{1}{4}\mathrm{e}^{-\beta z}(\mathrm{e}^{-\beta z} + 6\beta z\sin\beta z + 16\sin\beta z + 6\cos\beta z - 6\beta z\cos\beta z) - \frac{7}{4}\right)\\
&\quad - \frac{1}{2\omega}\left(\frac{\partial^2 u_\varphi^2}{\partial r^2}\right)\\
&\quad \times\left(\frac{1}{4}\mathrm{e}^{-\beta z}(\mathrm{e}^{-\beta z} + 2\beta z\sin\beta z + 8\sin\beta z + 2\cos\beta z - 2\beta z\cos\beta z) - \frac{3}{4}\right).
\end{aligned}\right\} \tag{2.45}$$

We compute the total circulation by detecting the vortex region using the d2 method, and then numerically integrating:

$$\Lambda = \sum_i \Lambda_i = \sum_i \Omega_i \Delta r\Delta z = \sum_i \left(\frac{\partial\langle w^{(2)}\rangle_t}{\partial r} - \frac{\partial\langle u^{(2)}\rangle_t}{\partial z}\right)\Delta r\Delta z, \tag{2.46}$$

which can be non-dimensionalized by $R_0^2\omega$ to obtain the non-dimensional circulation Λ^*.

3. Results and discussion

3.1. *Microstreaming due to free bubble oscillation*

Although the analysis delineated here is valid for different bubble radius and excitation parameters, we are primarily interested in microbubble-based contrast-enhanced ultrasound imaging and drug delivery applications with R_0 of the order of micrometres

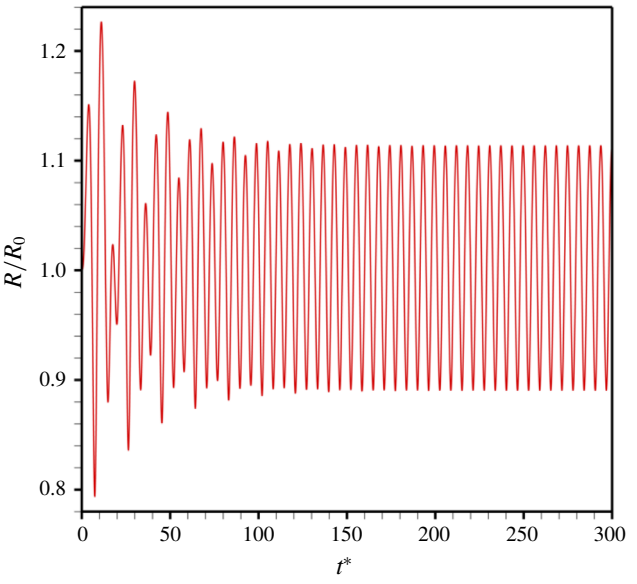

FIGURE 2. (Colour online) The radial pulsation of the free microbubble when $Re_b = 48$, $Eu_b = 0.11$, $We_b = 20$, $h/R_0 = 2$.

and f_{ex} in the megahertz range. Specifically, we consider the case of $R_0 = 1.6$ μm, the average radius of the contrast agent Sonazoid (Sontum *et al.* 1999; Sontum 2008), at an excitation frequency of 3 MHz. The driving amplitude was chosen to be small enough, $P_{ex} = 70$ kPa ($P^*_{ex} = 0.7$), to ensure linear oscillation, giving rise to $Re_b = 48$, $Eu_b = 0.11$ and $We_b = 20$. Figure 2 shows the radial pulsation of the microbubble with non-dimensional time located at $h = 2R_0$ obtained solving the full Rayleigh–Plesset equation (2.31) using a standard Matlab solver, ode15s. The eventual periodic oscillation with a non-dimensional amplitude $\varepsilon = 0,\ 11$ seen here is also predicted by the linearized form (2.35) demonstrating that the excitation is small enough for linear dynamics, and the linear analysis is valid. Note that the bubble streaming Reynolds number $Re_{bs} = \varepsilon^2(2Re_b)^{1/2} = 0.12$. We also check the approximation made in neglecting the z-variation of u^*_φ (varying in a scale R_0) inside the boundary layer.

In figure 3, we plot u^*_φ at $z = 0$ and at $z = \delta$ for three different separations $h = 1.5R_0$, $h = 2R_0$ and $h = 3R_0$. We note that the variation is small for all cases, being largest for the smallest separation $h = 1.5R_0$. Therefore the approximation adopted here – $u^*_\varphi(z = 0)$ and $\partial u^*_\varphi(z = 0)$ in (2.36) and (2.37) – following Nyborg (1958) is justified. The average streaming velocity (2.22) and (2.23) can be written in terms of the irrotational component of the first-order oscillating velocity u^*_φ. Figure 4 shows the streamlines of u^*_φ surrounding the microbubble at two different non-dimensional times corresponding to microbubble expansion and compression.

We plot the streamlines of microstreaming velocities $\langle u^{(2)}\rangle_t$ and $\langle w^{(2)}\rangle_t$ according to equations (2.22) and (2.23) in figures 5(*a*) and 5(*b*) for two locations of the microbubble at $h = 2R_0$ and $h = 3R_0$, respectively. This case is the same one discussed before for $\mathrm{Re}_b = 48$, $Eu_b = 0.11$, $We_b = 20$. They show the cross-sectional plot of the axisymmetric ring vortex over the wall. Inside the vortex, the flow near the wall is directed radially outward, while it is directed inward beyond the vortex length. The

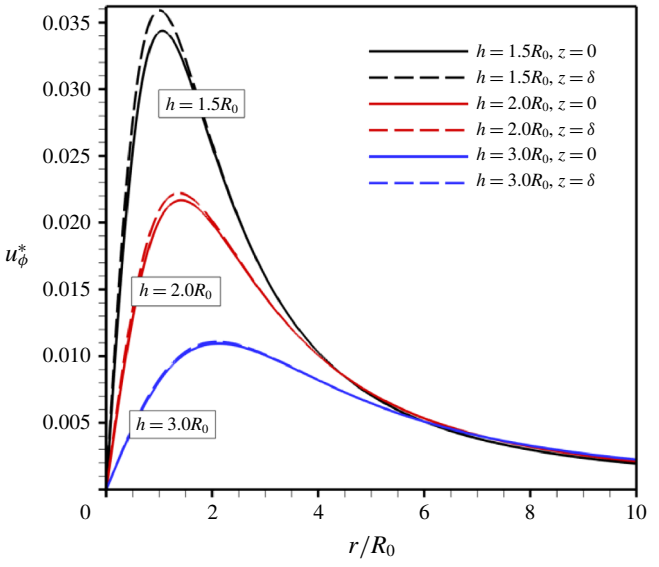

FIGURE 3. (Colour online) The non-dimensional irrotational velocity at $z = 0$ and $z = \delta$ for $h = 1.5R_0$, $h = 2R_0$, $h = 3R_0$ when $Re_b = 48$, $Eu_b = 0.11$, $We_b = 20$, $P^*_{ex} = 0.7$.

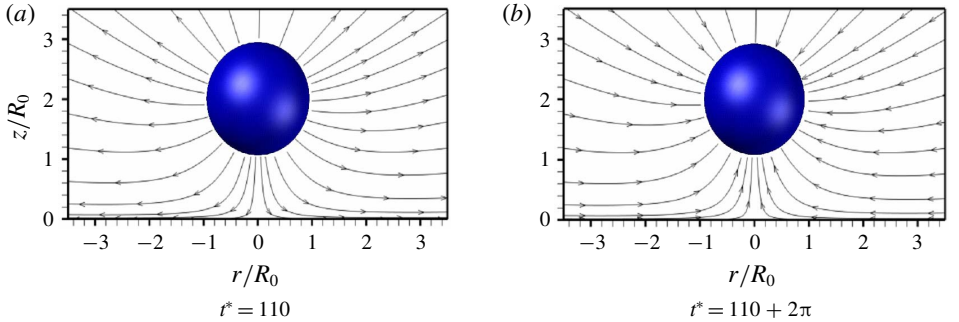

FIGURE 4. (Colour online) The irrotational velocity around the free microbubble when $Re_b = 48$, $Eu_b = 0.11$, $We_b = 20$, $h/R_0 = 2$, $P^*_{ex} = 0.7$: (*a*) expansion; (*b*) compression.

vortex ring extends up to $r^* = 1.41$ and $r^* = 2.12$ defining l_{vortex} along the wall for the cases $h = 2R_0$ and $h = 3R_0$ respectively. Length l_{vortex} increases with $h^* = h/R_0$.

To understand the generation of the vortex we examine (2.2) showing $\rho\langle \boldsymbol{u}^{(1)} \cdot \boldsymbol{\nabla} \boldsymbol{u}^{(1)} \rangle_t$ driving the Stokes equation for the streaming velocity. In particular, one sees that F_r in (2.20) is primarily dominated by the first term proportional to $u^*_\varphi \partial_r u^*_\varphi$ (the second term proportional to βz is small and zero at the wall). We plot u^*_φ and $\partial_r u^*_\varphi$ in figures 5(*c*) and 5(*d*) for the same cases as in figures 5(*a*) and 5(*b*). We see that the former achieves a peak and the latter changes sign at $r^* = 1.41$ and $r^* = 2.12$, resulting in F_r changing sign at those radial distances. This in turn changes the direction of $\langle u^{(2)} \rangle_t$ along the wall at these locations signalling the radial extent of the vortex l_{vortex}. In fact, one finds from (2.36)

$$\left.\frac{\partial u^*_\varphi}{\partial r^*}\right|_{z^*=0} = 0 \rightarrow \frac{l_{vortex}}{R_0} = \frac{h}{\sqrt{2}R_0}. \tag{3.1}$$

Note that this expression is independent of all other parameters and primarily results from the functional dependence in (2.36) arising due to the reflection from the wall. It matches with the values found above: $l_{vortex} = 1.41R_0$ and $2.12R_0$ for $h = 2R_0$ and $h = 3R_0$ respectively. In contrast to the vortex length, its vertical extent d_{vortex} remains unchanged with varying h, the microbubble separation from the wall ($0.32R_0$ for both $h^* = h/R_0 = 2$ and $h^* = 3$). It is of the order $\sim\delta$, the boundary layer thickness. One can compute it by considering the vertical component of streaming velocity close to the axis of symmetry being zero $\langle w^{(2)}\rangle_t(r^* \to 0, d_{vortex}/R_0) = 0$. Near the axis of symmetry where $r = 0$, one can approximate

$$\frac{\partial^2 u_\varphi^2}{\partial r^2} \simeq \mathrm{Lim}_{r\to 0}\frac{1}{r}\left(\left.\frac{\partial^2 u_\varphi^2}{\partial r^2}\right|_r - \left.\frac{\partial^2 u_\varphi^2}{\partial r^2}\right|_0\right) = \mathrm{Lim}_{r\to 0}\,\frac{1}{r}\left.\frac{\partial^2 u_\varphi^2}{\partial r^2}\right|_r . \tag{3.2}$$

Therefore, close to the axis, one can write (2.23) as

$$\langle w^{(2)}\rangle_t \simeq -\frac{1}{2\omega}\left(\frac{1}{r}\frac{\partial u_\varphi^2}{\partial r}\right) \times\left(-\frac{1}{4\beta}\mathrm{e}^{-2\beta z} - \frac{1}{4\beta}\mathrm{e}^{-\beta z}(8\beta z\sin\beta z + 12\sin\beta z + 20\cos\beta z) - \frac{10}{4}z + \frac{42}{8\beta}\right). \tag{3.3}$$

One then obtains

$$\langle w^{(2)}\rangle_t = 0 \to \frac{d_{vortex}}{R_0} = \frac{1.6}{R_0\beta} = 1.6\frac{\delta}{R_0} = \frac{1.6}{R_0}\sqrt{\frac{2\nu}{\omega}} = \frac{1.6\sqrt{2}}{\sqrt{Re_b}}. \tag{3.4}$$

Here, it results in $d_{vortex} = 0.32R_0$ as seen in figure 5(*a*,*b*). The width therefore is typical of boundary layer scaling and depends only on the excitation frequency and kinematic viscosity of the fluid.

Figures 5(*e*) and 5(*f*) show the shear stress on the wall induced by the microstreaming flow shown in figures 5(*a*) and 5(*b*), respectively. It changes sign at $r = l_{vortex}$ where the radial first-order irrotational velocity achieves its maximum. The maximum shear stress on the wall, as expected, decreases when the microbubble is excited further away from the wall. The value of the maximum shear stress appears at a distance $r^*_{max\,stress}$. One can take the expression (2.38) and find its maximum at $r^*_{max\,stress} = 0.2865h^*$ as was also found by Doinikov & Bouakaz (2010*a*,*b*). For the conditions investigated here ($R_0 = 1.6$ μm, $f_{ex} = 3$ MHz, $P_{ex} = 70$ kPa), the maximum shear stress is computed to be 12.8 and 2.2 Pa (note that $P_0 = 10^5$ Pa) from figure 5(*e*,*f*). We noted before that an average streaming shear stress expression $\tau_L = \mu u_L/\delta$ has been widely used in the literature to estimate the maximum shear stress on the wall induced by microstreaming. In figure 5(*e*,*f*) the non-dimensional average streaming shear stress τ_L^* (non-dimensionalized with respect to the ambient pressure) on the wall has been calculated using the limiting streaming velocity u_L ($z \to \infty$ in (2.38))

$$u_L = -\frac{1}{\omega}\left(\frac{3}{8}\frac{\partial u_\varphi^2}{\partial r} + \frac{u_\varphi^2}{2r}\right). \tag{3.5}$$

Note also that the direction of the radial limiting velocity is opposite to that of the radial microstreaming velocity close to the wall as can also be observed from the microstreaming streamlines in the regions close to and far from the wall. Therefore,

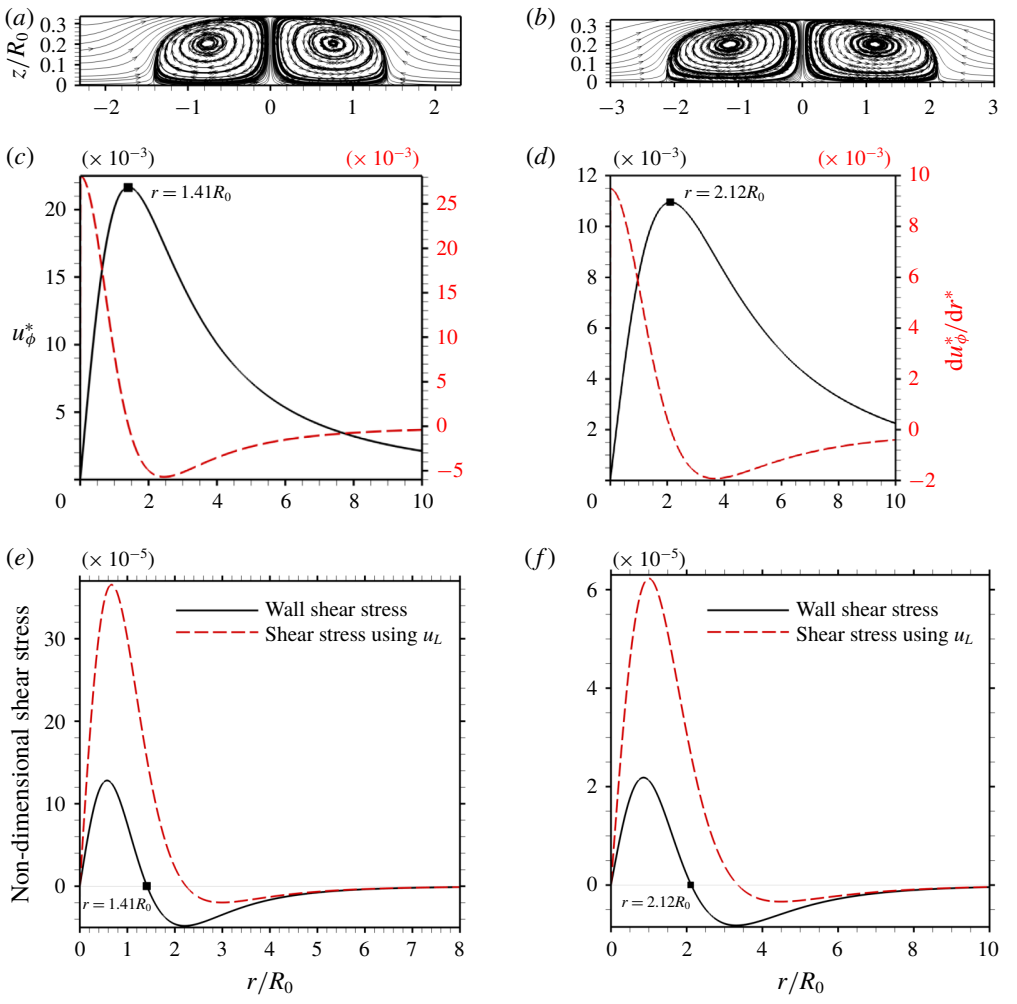

FIGURE 5. (Colour online) Microstreaming streamlines near the plane rigid wall when $Re_b = 48$, $Eu_b = 0.11$, $We_b = 20$, $P^*_{ex} = 0.7$ and the microbubble is located at (*a*) $h/R_0 = 2$ and (*b*) $h/R_0 = 3$. (*c*,*d*) Corresponding non-dimensional amplitude of radial potential velocity (black solid line) on the rigid wall and its derivative (red dashed line) with respect to radial distance along the wall. (*e*,*f*) Corresponding non-dimensional shear stress on the wall using limiting streaming velocity and microstreaming velocity.

opposite sign has been chosen for computing τ^*_L and compared to the wall stress. In any event, τ^*_L which is often used in the literature is computed to be much higher (almost three times in figure 5*e*,*f*) than the wall shear stress.

Observing the motion of the tracer particles to delineate microstreaming, one obtains the Lagrangian streamlines. Figure 6 compares Lagrangian with Eulerian streamline patterns demonstrating that for the same flow field they are significantly different. Specifically, the vertical width of the vortical structure is narrower in the Lagrangian field causing the Lagrangian velocity to be of opposite sign at the same position. In figure 7, we plot the radial and vertical velocity components in both Eulerian and Lagrangian descriptions at three different vertical locations $z = 0.03R_0$,

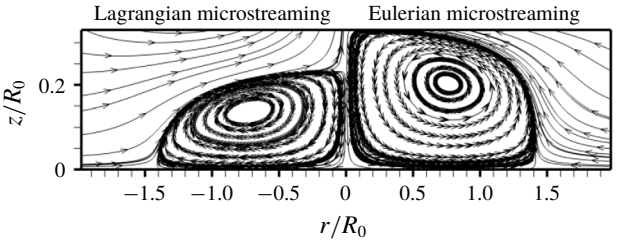

FIGURE 6. Comparing microstreaming streamlines near the plane rigid wall due to a free microbubble using Lagrangian and Eulerian streaming when $Re_b = 48$, $Eu_b = 0.11$, $We_b = 20$, $h/R_0 = 2$, $P^*_{ex} = 0.7$.

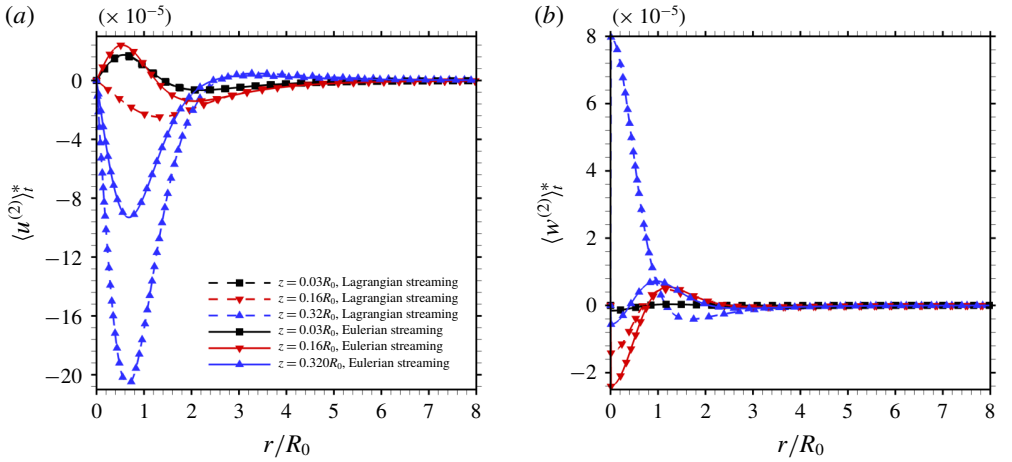

FIGURE 7. (Colour online) Comparing (*a*) radial component and (*b*) vertical component of Lagrangian and Eulerian microstreaming velocity at three different vertical distances $z = 0.03R_0$, $z = 0.16R_0$ and $z = 0.32R_0$ from the wall when $Re_b = 48$, $Eu_b = 0.11$, $We_b = 20$, $h/R_0 = 2$, $P^*_{ex} = 0.7$.

$z = 0.16R_0$ and $z = 0.32R_0$ from the wall. We find that the velocities in the two different descriptions are similar and in the same direction closest to the wall, but at $z = 0.125R_0$, while Eulerian radial velocity is positive, i.e. outward close to the axis in the bottom region of the vortex, its Lagrangian counterpart is mostly negative in the top part of the Lagrangian vortex (figure 7*a*). The vertical velocity in figure 7(*b*) shows similar differences in the two descriptions. Note that the highest magnitude of the radial Eulerian velocity at $z = 0.32R_0$ (top of the vortex) is ~ 3 mm s^{-1}.

We have examined the effects of bubble translational motion on the theoretical expression of microstreaming in § 2.6 noting that the effects are small. In figure 8, we validate this conclusion by noting that accounting for translation leads to very little change in the streamline pattern.

Figure 9 plots the vorticity. The region of high negative vorticity (on the right-hand side of the figure; the left-hand side is antisymmetric) in the area adjoining the wall is generated by the strong shear due to the no-slip condition, coinciding with the flatter streamlines in the lower part of the vortex (figure 8). The vorticity increases with vertical distance from the wall changing sign to become positive and achieving the

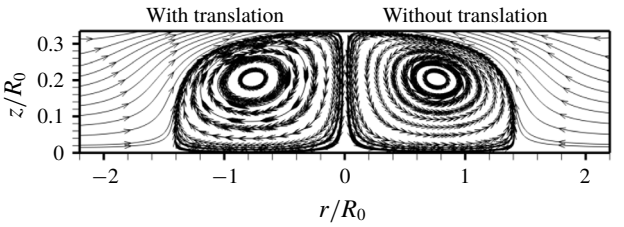

FIGURE 8. Streamlines due to microstreaming near the plane rigid wall due to a free microbubble with and without accounting for translational motion when $Re_b = 48$, $Eu_b = 0.11$, $We_b = 20$, $h/R_0 = 2$, $P^*_{ex} = 0.7$.

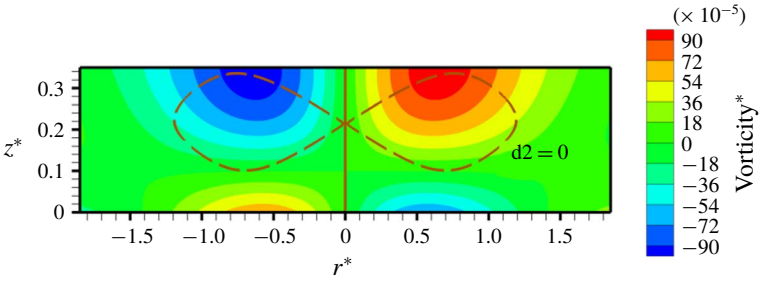

FIGURE 9. (Colour online) Vorticity contours due to the ring vortex induced by free microbubble when $Re_b = 48$, $Eu_b = 0.11$, $We_b = 20$ at $h/R_0 = 2$, $P^*_{ex} = 0.7$.

highest positive value near the edge of the vortex flow due to the strong shear layer there. The vorticity field, although generated by the vortex flow, does not provide an easy identification of the vortex, embodying the problem of vortex identification described in § 2.8. We identify the vortex region using the d2 method – inside the region enclosed by the $d_2 = 0$ curve in figure 9, where d_2 according to (2.44) is negative – and compute circulation of the vortex. We note that the region identified by the d2 method is smaller than what can be estimated from the streamline plot in figure 8. The closely spaced straight streamlines near the boundaries of the vortex in figure 8 were identified by the method as due to the boundary shear rather than due to the vortex. As described before, such difficulties of vortex identification methods have been discussed before in the literature (Chakraborty *et al.* 2005). However, the vortex identified allows us to compute the circulation. Figure 10(*a*) shows the non-dimensional circulation Λ^* of the axisymmetric vortex ring (non-dimensionalized by $R_0^2\omega$) as a function of separation distance h of the microbubble from the wall. We also plot the maximum shear stress τ^*_{max} in the same figure. They both decrease with increasing separation of the microbubble from the wall with a power-law variation with h/R_0.

We investigate these variations in detail. In order to accommodate widely different magnitudes of these quantities in the same figure, we plot in figure 10(*b*) these quantities – circulation, maximum shear stress – by normalizing them by their highest values occurring at $h/R_0 = 1$, i.e. $\Lambda^*(h/R_0 = 1)$ and $\tau^*_{max}(h/R_0 = 1)$. We also plot maximum vorticity Ω_{max} normalizing it by $\Omega_{max}(h/R_0 = 1)$. We note similar scaling in shear stress and vorticity τ^*_{max}, $\Omega_{max} \sim (h/R_0)^{-4.3}$. This can be explained by noting that the term $\partial\langle u_2\rangle/\partial y$ responsible for τ is the dominant part in Ω. We find

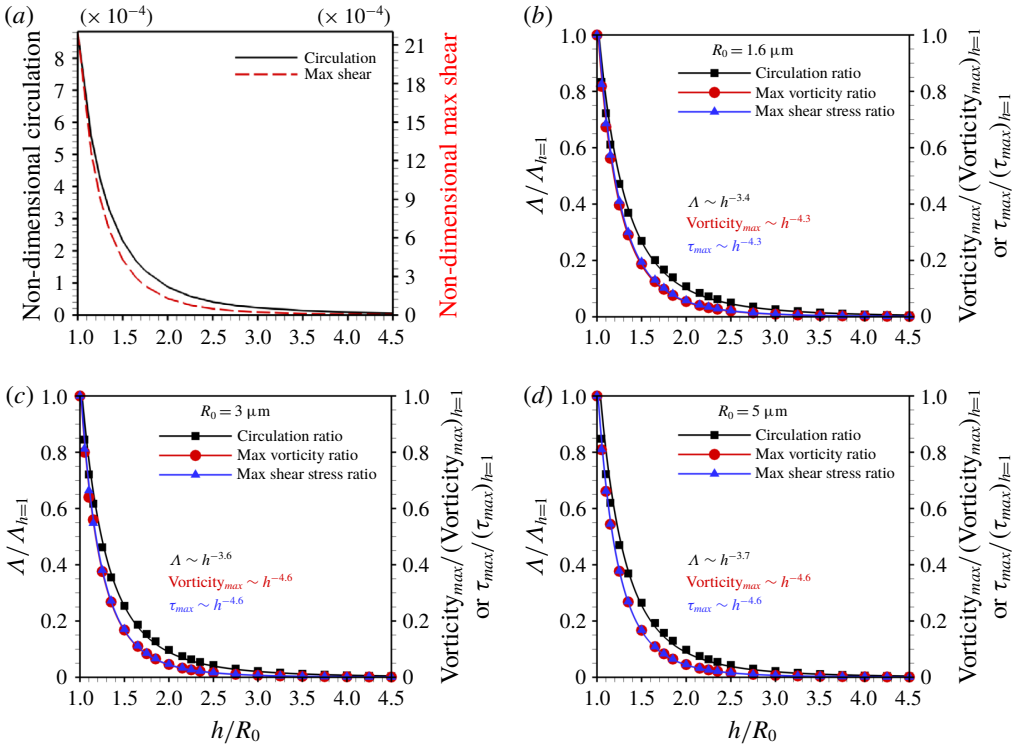

FIGURE 10. (Colour online) (*a*) Non-dimensional circulation of the ring vortex and non-dimensional maximum shear stress as a function of the separation distance of the microbubble from the wall when $Re_b = 48$, $Eu_b = 0.11$, $We_b = 20$, $P^*_{ex} = 0.7$. (*b*) Circulation, maximum vorticity and maximum wall shear stress normalized by their values at $h/R_0 = 1$ as a function of h/R_0 for the same condition as in (*a*). (*c*) The same quantities as plotted in (*b*) for $Re_b = 170$, $Eu_b = 0.03$, $We_b = 133$. (*d*) The same quantities as plotted in (*b*) for $Re_b = 471$, $We_b = 617$, $Eu_b = 0.011$.

$\Lambda^* \sim (h/R_0)^{-3.4}$. Approximate relation $\Lambda^* \sim \Omega_{max}(h/R_0)$ can be explained by noting the Stokes theorem $\Lambda = \int \Omega \, dr \, dz \sim \Omega_{max} l_{vortex} d_{vortex}$ and the relations found before (3.1) and (3.4). These relations are also seen for other microbubble radii $R_0 = 3$ μm and $R_0 = 5$ μm (correspondingly different Re_b, Eu_b and We_b) in figures 10(*c*) and 10(*d*). The exact power-law indices differ but τ^*_{max} and Ω_{max} have the same index and $\Lambda^* \sim \Omega_{max}(h/R_0)$ approximately holds in all cases.

3.2. *Effects of microbubble coating on microstreaming*

Here we consider the effects of the stabilizing coating on a microbubble. As noted before, we consider the contrast agent Sonazoid and use its property values determined using the exponential elasticity model (Paul *et al.* 2010): $\gamma_0 = 0.019$ N m^{-1}, $E^s_0 = 0.55$ N m^{-1}, $\alpha^s = 1.5$ and $\kappa^s = 1.2 \times 10^{-8}$ N s m^{-1}. Note that we found qualitatively similar results with other models (not shown here) such as that of Marmottant *et al.* (2005). We choose bubble radius of 1.6 μm, average size of Sonazoid $h = 2R_0$ and identical excitation parameters (70 kPa, 3 MHz) as before giving rise to $Re_b = 48$, $Eu_b = 0.11$, $We_b = 20$, $Re^s_b = 6.4$, $We^s_b = 2.6$. Two

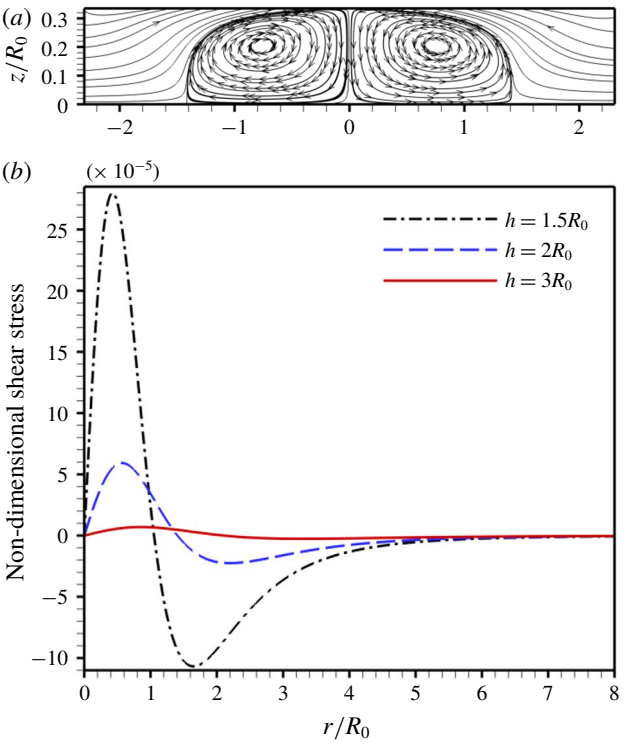

FIGURE 11. (Colour online) (*a*) Streaming velocity field near the plane rigid wall due to coated microbubble when $Re_b = 48$, $Eu_b = 0.11$, $We_b = 20$, $Re_b^s = 6.4$, $We_b^s = 2.6$, $h/R_0 = 2$, $\gamma_0/E_0^s = 0.0345$ and $\alpha^s = 1.5$. (*b*) Wall shear stress for the same conditions as well as for two other values of h/R_0.

material non-dimensional parameters are $\gamma_0/E_0^s = 0.0345$ and $\alpha^s = 1.5$. Resulting non-dimensional periodic oscillation amplitude is $\varepsilon = 0.08$, smaller than the free bubble. The bubble streaming Reynolds number $Re_{bs} = 0.06$ is also correspondingly smaller. Figure 11(*a*) shows the microstreaming streamlines due to a pulsating Sonazoid microbubble for this condition. The streamline pattern is similar to that due to a free microbubble without any coating shown in figure 4(*a*). The dimensions of the vortex $l_{vortex} = 1.41R_0$ and $d_{vortex} = 0.32R_0$ are the same as those in free vortex (as determined, for example, by equation (3.1)). In figure 11(*b*), we show the wall shear stress for the same condition. Shear stress profiles are similar to those for a free bubble, reaching zero value at $r^* = l_{vortex}/R_0$. The value of the maximum shear stress for this coated bubble is 6 Pa, smaller than the case of a free bubble for the same conditions (size, excitation parameters and separation) with identical position and the shear stress expectedly decreases and with increasing bubble separation; at the same time, l_{vortex} increases as per equation (3.1).

To examine the effects of the shell parameters, in figures 12(*a*) and 12(*b*) we plot the non-dimensional circulation of the vortex Λ^* and non-dimensional maximum shear stress on the wall with respect to shell viscosity ratio $\kappa^s/\kappa^s_{(sonazoid)}$ and shell elasticity ratio $E_0^s/E^s_{0(sonazoid)}$, respectively, with other parameters held the same as before. The values for Sonazoid coating agent are $E^s_{0(sonazoid)} = 0.55$ N m^{-1} and $\kappa^s_{sonazoid} = 1.2 \times 10^{-8}$ N s m^{-1}. Here Λ^* and τ^*_{max} show identical variations with coating parameters.

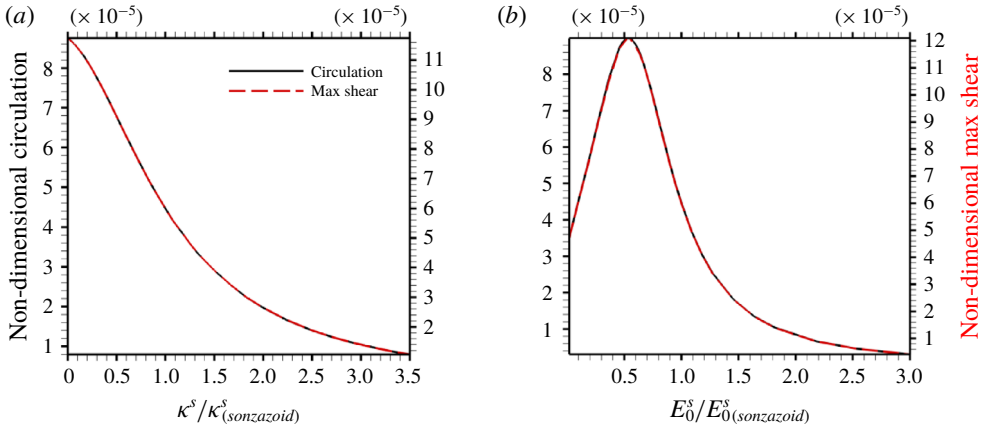

FIGURE 12. (Colour online) Non-dimensional circulation of half the ring vortex and maximum wall shear stress due to coated microbubble (*a*) with respect to dilatation viscosity and (*b*) with respect to coating elasticity when $Re_b = 48$, $Eu_b = 0.11$, $We_b = 20$, $h/R_0 = 2$ and $\alpha^s = 1.5$.

Coating parameters affect the bubble pulsation amplitude and that in turn affects Λ^* and τ^*_{max}. The variations in Λ^* and τ^*_{max} are then identical for the same reasons as for the free bubble. Figure 12(*a*) shows that circulation and maximum shear stress decrease with increasing dilatational viscosity, as can be expected from the fact that at higher dilatational viscosities, the coated microbubble has smaller pulsation amplitudes and thereby lower streaming velocity and lower shear stress as well as circulation. The change of circulation and shear stress with shell elasticity (figure 12*b*) shows a maximum corresponding to $E^s_0 = 0.27$ N m^{-1}. The maximum signals a resonance of the coated microbubble at the excitation frequency; changing the shell elasticity changes the spring constant and correspondingly the resonance frequency of the coated bubble according to equation (2.43), i.e. the oscillation is maximum at this value of E^s_0.

4. Conclusion

Acoustic microstreaming due to an oscillating bubble near a plane wall has been analytically investigated in detail using a perturbative theory. Both free and coated microbubbles have been considered. The Eulerian and Lagrangian velocity fields and wall shear stresses have been computed. The closed streamlines of the axisymmetric ring vortex have been plotted. The vortex geometry has been identified using a d2 method and its circulation computed. Under the approximations used, the vortex radial length along the wall is found to depend only on the separation of the bubble from the wall with the dependence being linear. The maximum shear stress has been shown to have the same variation with bubble separation as the circulation. For coated microbubbles, a strain-softening viscoelastic interfacial model for the coating is used. The analytical results for the coated bubble are similar to those for the free bubble. The wall shear stress decreases with increasing shell dilatational viscosity and shows a non-monotonic behaviour with increasing shell dilatational elasticity with a peak at the resonance.

Acknowledgements

K.S. acknowledges partial support from NSF CBET 1602884, and George Washington University. The authors acknowledge important suggestions from and fruitful discussions with Drs K. Bulusu and M. R. Najjari regarding the d2 methods and with Professor Rallabandi regarding experiments of acoustic streaming.

REFERENCES

ALIABOUZAR, M., LEE, S. J., ZHOU, X., ZHANG, G. L. J. & SARKAR, K. 2018 Effects of scaffold microstructure and low intensity pulsed ultrasound on chondrogenic differentiation of human mesenchymal stem cells. *Biotechnol. Bioengng* **115** (2), 495–506.

ALIABOUZAR, M., ZHANG, L. G. & SARKAR, K. 2016 Lipid coated microbubbles and low intensity pulsed ultrasound enhance chondrogenesis of human mesenchymal stem cells in 3D printed scaffolds. *Sci. Rep.* **6**, 37728.

BATCHELOR, G. K. 1967 *An Introduction to Fluid Dynamics*. Cambridge University Press.

CHAKRABORTY, P., BALACHANDAR, S. & ADRIAN, R. J. 2005 On the relationships between local vortex identification schemes. *J. Fluid Mech.* **535**, 189–214.

CHATTERJEE, D. & SARKAR, K. 2003 A Newtonian rheological model for the interface of microbubble contrast agents. *Ultrasound Med. Biol.* **29** (12), 1749–1757.

CHURCH, C. C. 1995 The effects of an elastic solid-surface layer on the radial pulsations of gas-bubbles. *J. Acoust. Soc. Am.* **97** (3), 1510–1521.

COLLIS, J., MANASSEH, R., LIOVIC, P., THO, P., OOI, A., PETKOVIC-DURAN, K. & ZHU, Y. 2010 Cavitation microstreaming and stress fields created by microbubbles. *Ultrasonics* **50** (2), 273–279.

DAVIDSON, B. J. & RILEY, N. 1971 Cavitation microstreaming. *J. Sound Vib.* **15** (2), 217–233.

DOINIKOV, A. A. & BOUAKAZ, A. 2010*a* Acoustic microstreaming around a gas bubble. *J. Acoust. Soc. Am.* **127** (2), 703–709.

DOINIKOV, A. A. & BOUAKAZ, A. 2010*b* Theoretical investigation of shear stress generated by a contrast microbubble on the cell membrane as a mechanism for sonoporation. *J. Acoust. Soc. Am.* **128** (1), 11–19.

DOINIKOV, A. A. & BOUAKAZ, A. 2014 Effect of a distant rigid wall on microstreaming generated by an acoustically driven gas bubble. *J. Fluid Mech.* **742**, 425–445.

DOINIKOV, A. A. & BOUAKAZ, A. 2016 Microstreaming generated by two acoustically induced gas bubbles. *J. Fluid Mech.* **796**, 318–339.

ELDER, S. A. 1959 Cavitation microstreaming. *J. Acoust. Soc. Am.* **31** (1), 54–64.

FABRE, D., JALAL, J., LEONTINI, J. S. & MANASSEH, R. 2017 Acoustic streaming and the induced forces between two spheres. *J. Fluid Mech.* **810**, 378–391.

FAN, Z., KUMON, R. E. & DENG, C. X. 2014 Mechanisms of microbubble-facilitated sonoporation for drug and gene delivery. *Therapeutic Deliv.* **5** (4), 467–486.

FORBES, M. M. & O'BRIEN, W. D. JR 2012 Development of a theoretical model describing sonoporation activity of cells exposed to ultrasound in the presence of contrast agents. *J. Acoust. Soc. Am.* **131** (4), 2723–2729.

GOLDBERG, B. B., RAICHLEN, J. S. & FORSBERG, F. 2001 *Ultrasound Contrast Agents: Basic Principles and Clinical Applications*. Martin Dunitz.

HOFF, L., SONTUM, P. C. & HOVEM, J. M. 2000 Oscillations of polymeric microbubbles: effect of the encapsulating shell. *J. Acoust. Soc. Am.* **107** (4), 2272–2280.

DE JONG, N., CORNET, R. & LANCEE, C. T. 1994 Higher harmonics of vibrating gas-filled microspheres. 1. Simulations. *Ultrasonics* **32** (6), 447–453.

DE JONG, N., HOFF, L., SKOTLAND, T. & BOM, N. 1992 Absorption and scatter of encapsulated gas filled microspheres – theoretical considerations and some measurements. *Ultrasonics* **30** (2), 95–103.

KATIYAR, A., DUNCAN, R. L. & SARKAR, K. 2014 Ultrasound stimulation increases proliferation of MC3T3-E1 preosteoblast-like cells. *J. Theor. Ultrasound* **2**, 1.

KATIYAR, A. & SARKAR, K. 2011 Excitation threshold for subharmonic generation from contrast microbubbles. *J. Acoust. Soc. Am.* **130** (5), 3137–3147.

KATIYAR, A., SARKAR, K. & JAIN, P. 2009 Effects of encapsulation elasticity on the stability of an encapsulated microbubble. *J. Colloid Interface Sci.* **336**, 519–525.

KOLB, J. & NYBORG, W. L. 1956 Small-scale acoustic streaming in liquids. *J. Acoust. Soc. Am.* **28** (6), 1237–1242.

KRASOVITSKI, B. & KIMMEL, E. 2004 Shear stress induced by a gas bubble pulsating in an ultrasonic field near a wall. *IEEE Trans. Ultrason. Ferroelectr. Freq. Control* **51** (8), 973–979.

KUMAR, K. N. & SARKAR, K. 2015 Effects of ambient hydrostatic pressure on the material properties of the encapsulation of an ultrasound contrast microbubble. *J. Acoust. Soc. Am.* **138** (2), 624–634.

KUMAR, K. N. & SARKAR, K. 2016 Interfacial rheological properties of contrast microbubble Targestar P as a function of ambient pressure. *Ultrasound Med. Biol.* **42** (4), 1010–1017.

LAJOINIE, G., LUAN, Y., GELDERBLOM, E., DOLLET, B., MASTIK, F., DEWITTE, H., LENTACKER, I., DE JONG, N. & VERSLUIS, M. 2018 Non-spherical oscillations drive the ultrasound-mediated release from targeted microbubbles. *Commun. Phys.* **1** (1), 22.

LENTACKER, I., DE SMEDT, S. C. & SANDERS, N. N. 2009 Drug loaded microbubble design for ultrasound triggered delivery. *Soft Matt.* **5** (11), 2161–2170.

LEWIN, P. A. & BJORNO, L. 1982 Acoustically induced shear stresses in the vicinity of microbubbles in tissue. *J. Acoust. Soc. Am.* **71** (3), 728–734.

LIGHTHILL, J. 1978 Acoustic streaming. *J. Sound Vib.* **61** (3), 391–418.

LIU, X. & WU, J. 2009 Acoustic microstreaming around an isolated encapsulated microbubble. *J. Acoust. Soc. Am.* **125** (3), 1319–1330.

MARMOTTANT, P. & HILGENFELDT, S. 2003 Controlled vesicle deformation and lysis by single oscillating bubbles. *Nature* **423** (6936), 153–156.

MARMOTTANT, P., VAN DER MEER, S., EMMER, M., VERSLUIS, M., DE JONG, N., HILGENFELDT, S. & LOHSE, D. 2005 A model for large amplitude oscillations of coated bubbles accounting for buckling and rupture. *J. Acoust. Soc. Am.* **118** (6), 3499–3505.

MILLER, D. L. 1988 Particle gathering and microstreaming near ultrasonically activated gas-filled micropores. *J. Acoust. Soc. Am.* **84** (4), 1378–1387.

MOBADERSANY, N. & SARKAR, K. 2018 Collapse and jet formation of ultrasound contrast microbubbles near a membrane for sonoporation. In *10th International Cavitation Symposium, Baltimore, MD, USA*. ASME.

NAJJARI, M. R. & PLESNIAK, M. W. 2016 Evolution of vortical structures in a curved artery model with non-Newtonian blood-analog fluid under pulsatile inflow conditions. *Exp. Fluids* **57** (6), 100.

NYBORG, W. L. 1953 Acoustic streaming due to attenuated plane waves. *J. Acoust. Soc. Am.* **25** (1), 68–75.

NYBORG, W. L. 1958 Acoustic streaming near a boundary. *J. Acoust. Soc. Am.* **30** (4), 329–339.

ORBAY, S., OZCELIK, A., LATA, J., KAYNAK, M., WU, M. & HUANG, T. J. 2016 Mixing high-viscosity fluids via acoustically driven bubbles. *J. Micromech. Microengng* **27** (1), 015008.

PAUL, S., KATIYAR, A., SARKAR, K., CHATTERJEE, D., SHI, W. T. & FORSBERG, F. 2010 Material characterization of the encapsulation of an ultrasound contrast microbubble and its subharmonic response: strain-softening interfacial elasticity model. *J. Acoust. Soc. Am.* **127** (6), 3846–3857.

PAUL, S., NAHIRE, R., MALLIK, S. & SARKAR, K. 2014 Encapsulated microbubbles and echogenic liposomes for contrast ultrasound imaging and targeted drug delivery. *Comput. Mech.* **53** (3), 413–435.

PAUL, S., RUSSAKOW, D., RODGERS, T., SARKAR, K., COCHRAN, M. & WHEATLEY, M. A. 2013 Determination of the interfacial rheological properties of a poly(DL-lactic acid)-encapsulated contrast agent using in vitro attenuation and scattering. *Ultrasound Med. Biol.* **39** (7), 1277–1291.

POMMELLA, A., BROOKS, N. J., SEDDON, J. M. & GARBIN, V. 2015 Selective flow-induced vesicle rupture to sort by membrane mechanical properties. *Sci. Rep.* **5**, 13163.

RALLABANDI, B., MARIN, A., ROSSI, M., KAHLER, C. J. & HILGENFELDT, S. 2015 Three-dimensional streaming flow in confined geometries. *J. Fluid Mech.* **777**, 408–429.

RALLABANDI, B., WANG, C. & HILGENFELDT, S. 2014 Two-dimensional streaming flows driven by sessile semicylindrical microbubbles. *J. Fluid Mech.* **739**, 57–71.

RANEY, W. P., CORELLI, J. C. & WESTERVELT, P. J. 1954 Acoustical streaming in the vicinity of a cylinder. *J. Acoust. Soc. Am.* **26** (6), 1006–1014.

RAYLEIGH, L. 1945 *Theory of Sound*. Dover.

RILEY, N. 2001 Steady streaming. *Annu. Rev. Fluid Mech.* **33** (1), 43–65.

ROONEY, J. A. 1970 Hemolysis near an ultrasonically pulsating gas bubble. *Science* **169** (3948), 869–871.

SARKAR, K., KATIYAR, A. & JAIN, P. 2009 Growth and dissolution of an encapsulated contrast microbubble. *Ultrasound Med. Biol.* **35** (8), 1385–1396.

SARKAR, K., SHI, W. T., CHATTERJEE, D. & FORSBERG, F. 2005 Characterization of ultrasound contrast microbubbles using in vitro experiments and viscous and viscoelastic interface models for encapsulation. *J. Acoust. Soc. Am.* **118** (1), 539–550.

SCHLICTING, H. 1979 *Boundary Layer Theory*. McGraw-Hill.

SONTUM, P. C. 2008 Physicochemical characteristics of Sonazoid^{TM}, a new contrast agent for ultrasound imaging. *Ultrasound Med. Biol.* **34** (5), 824–833.

SONTUM, P. C., OSTENSEN, J., DYRSTAD, K. & HOFF, L. 1999 Acoustic properties of NC100100 and their relation with the microbubble size distribution. *Investigative Radiol.* **34** (4), 268–275.

STUART, J. T. 1966 Double boundary layers in oscillatory viscous flow. *J. Fluid Mech.* **24**, 673–687.

THAMEEM, R., RALLABANDI, B. & HILGENFELDT, S. 2016 Particle migration and sorting in microbubble streaming flows. *Biomicrofluidics* **10** (1), 014124.

THO, P., MANASSEH, R. & OOI, A. 2007 Cavitation microstreaming patterns in single and multiple bubble systems. *J. Fluid Mech.* **576**, 191–233.

TSIGLIFIS, K. & PELEKASIS, N. A. 2008 Nonlinear radial oscillations of encapsulated microbubbles subject to ultrasound: the effect of membrane constitutive law. *J. Acoust. Soc. Am.* **123** (6), 4059–4070.

VOLLMERS, H. 2001 Detection of vortices and quantitative evaluation of their main parameters from experimental velocity data. *Meas. Sci. Technol.* **12** (8), 1199–1207.

WANG, C., JALIKOP, S. V. & HILGENFELDT, S. 2012 Efficient manipulation of microparticles in bubble streaming flows. *Biomicrofluidics* **6** (1), 012801.

WESTERVELT, P. J. 1953 The theory of steady rotational flow generated by a sound field. *J. Acoust. Soc. Am.* **25** (1), 60–67.

WU, J. & DU, G. 1997 Streaming generated by a bubble in an ultrasound field. *J. Acoust. Soc. Am.* **101** (4), 1899–1907.

WU, J. R. 2002 Theoretical study on shear stress generated by microstreaming surrounding contrast agents attached to living cells. *Ultrasound Med. Biol.* **28** (1), 125–129.

XIA, L., PORTER, T. M. & SARKAR, K. 2015 Interpreting attenuation at different excitation amplitudes to estimate strain-dependent interfacial rheological properties of lipid-coated monodisperse microbubbles. *J. Acoust. Soc. Am.* **138** (6), 3994–4003.

ZHOU, X., CASTRO, N. J., ZHU, W., CUI, H. T., ALIABOUZAR, M., SARKAR, K. & ZHANG, L. G. 2016 Improved human bone marrow mesenchymal stem cell osteogenesis in 3D bioprinted tissue scaffolds with low intensity pulsed ultrasound stimulation. *Sci. Rep.* **6**, 23876.